Stability of H_3O at extreme conditions and implications for the magnetic fields of Uranus and Neptune

Peihao Huang[a,b,1], Hanyu Liu[a,b,1], Jian Lv[a,b], Quan Li[a,b,c], Chunhong Long[d], Yanchao Wang[a,b,2], Changfeng Chen[e,2], Russell J. Hemley[f,g,2], and Yanming Ma[a,b,h,2]

[a]State Key Laboratory of Superhard Materials, College of Physics, Jilin University, 130012 Changchun, China; [b]International Center for Computational Methods and Software, College of Physics, Jilin University, 130012 Changchun, China; [c]Ministry of Education Key Laboratory of Automobile Materials, Department of Materials Science, Jilin University, 130012 Changchun, China; [d]School of Science, Chongqing University of Posts and Telecommunications, 400065 Chongqing, China; [e]Department of Physics and Astronomy, University of Nevada, Las Vegas, NV 89154; [f]Department of Physics, University of Illinois at Chicago, Chicago, IL 60607; [g]Department of Chemistry, University of Illinois at Chicago, Chicago, IL 60607; and [h]International Center of Future Science, Jilin University, 130012 Changchun, China

Contributed by Russell J. Hemley, January 8, 2020 (sent for review December 16, 2019; reviewed by Dennis D. Klug, Jonathan I. Lunine, and Chang Q. Sun)

The anomalous nondipolar and nonaxisymmetric magnetic fields of Uranus and Neptune have long challenged conventional views of planetary dynamos. A thin-shell dynamo conjecture captures the observed phenomena but leaves unexplained the fundamental material basis and underlying mechanism. Here we report extensive quantum-mechanical calculations of polymorphism in the hydrogen–oxygen system at the pressures and temperatures of the deep interiors of these ice giant planets (to >600 GPa and 7,000 K). The results reveal the surprising stability of solid and fluid trihydrogen oxide (H_3O) at these extreme conditions. Fluid H_3O is metallic and calculated to be stable near the cores of Uranus and Neptune. As a convecting fluid, the material could give rise to the magnetic field consistent with the thin-shell dynamo model proposed for these planets. H_3O could also be a major component in both solid and superionic forms in other (e.g., nonconvecting) layers. The results thus provide a materials basis for understanding the enigmatic magnetic-field anomalies and other aspects of the interiors of Uranus and Neptune. These findings have direct implications for the internal structure, composition, and dynamos of related exoplanets.

planetary science | high-pressure physics | magnetic fields | water

Planetary magnetic fields arise from magnetohydrodynamic processes (1). Earth's geomagnetic field is generated in its outer core, which consists largely of molten iron, whereas the magnetic fields of Jupiter and Saturn are produced within thick layers consisting predominantly of metallic fluid hydrogen. The magnetic fields of most planets in the Solar System are axial-dipole dominated; the exceptions are Uranus and Neptune, which exhibit anomalous nondipolar and nonaxisymmetric fields (2, 3). Interior models of these planets developed over the years generally identify three constituent regions, namely a gaseous hydrogen–helium outer envelope, a thick intermediate layer of "hot ices," and a core consisting of heavier elements (4). The pressure–temperature (P-T) conditions of the outer region are insufficient to produce fluid metallic hydrogen, and the proposed cores are thought to be solid or nonconvecting, which would preclude the existence of a dynamo in either region needed to produce the observed magnetic fields. The middle so-called "ice layer" has therefore been proposed as the region most likely to be responsible for the anomalous magnetic fields, specifically in a "thin" shell above the core (5, 6). Dynamo models have been proposed that are able to reproduce the anomalous nondipolar and nonaxisymmetric fields of Uranus and Neptune (7, 8), but a number of questions remain (9–11).

A fundamental question concerns their origin and physical mechanism of these intriguing planetary magnetic fields in terms of the component materials, an issue which in turn requires constraints on composition. The dearth of information about materials behavior at the relevant conditions has been cited as problematic for the thin-shell dynamo model in particular (11). A compositional reference model developed for these planets constrains the ice layer composition to have mole fractions of 56% H_2O, 36% CH_4, and 8% NH_3 (12), later refined as "synthetic Uranus" (13), with P-T conditions spanning 20–600 GPa and 2,000–7,000 K. CH_4 becomes unstable and dissociates into C and H_2 above 10 GPa and 2,000 K (14–18), and NH_3 is predicted to react with water to produce molecular mixtures in the form of $(H_2O)(NH_3)_2$ from 80 to 540 GPa (19). Assuming full dissociation of CH_4 and complete mixing of NH_3 with H_2O, the ice layers are expected to have H_2O:H_2 ratios reaching 13:18.

Given the large H_2O component, there has been a great deal of focus on the role of phases of H_2O in generating the magnetic fields within these planets. It has been suggested that H_2O in the form of superionic ice constitutes a large fraction of the ice layer with ionic fluid water in the outer portions (20–23). This proposal has led to a number of subsequent computational studies of the behavior of H_2O at high P-T conditions (24–27). The results found electrical conductivities of 2–20 $(\Omega\ \mathrm{cm})^{-1}$ in ionic H_2O ice and near 100 $(\Omega\ \mathrm{cm})^{-1}$ in superionic ice (3, 9). Although these species may contribute to magnetic field generation, it is important

Significance

Understanding the interior structure and dynamics of outer Solar System planets in terms of their component materials is a major scientific challenge. A highly intriguing case concerns the anomalous nondipolar and nonaxisymmetric magnetic fields of Uranus and Neptune. A thin-shell dynamo model has been shown to capture observed phenomena but leaves unexplained its origin and materials basis. We report extensive theoretical calculations that indicate the stability of trihydrogen oxide (H_3O) in solid, superionic, and fluid metallic states at the deep interior conditions of these planets. The fluid metallic phase is stable in a thin-shell zone near their cores and exhibits the properties required to produce the observed enigmatic magnetic fields. These findings have implications for other planets, including related exoplanets.

Author contributions: Y.W. and Y.M. conceived and designed the project; P.H., H.L., and Y.W. performed simulations; P.H., H.L., J.L., Q.L., C.L., Y.W., C.C., R.J.H., and Y.M. performed data analysis and interpretation of the results; H.L., Y.W., C.C., R.J.H., and Y.M. wrote the paper; and all authors contributed to discussions of the results and revisions of the manuscript.

Reviewers: D.D.K., National Research Council of Canada; J.I.L., Cornell University; and C.Q.S., Nanyang Technological University.

The authors declare no competing interest.

[1]P.H. and H.L contributed equally to this work.

[2]To whom correspondence may be addressed. Email: wyc@calypso.cn, chen@physics.unlv.edu, rhemley@uic.edu, or mym@jlu.edu.cn.

This article contains supporting information online at https://www.pnas.org/lookup/suppl/doi:10.1073/pnas.1921811117/-/DCSupplemental.

to consider the role of other high *P-T* phases in the H–O binary system.

There have been limited studies of the broader O–H binary system along the full range of *P-T* conditions of the deep interiors of Uranus and Neptune. High-pressure experiments on hydrogen and water have uncovered new phases, including the existence of H_4O which consists of the expected molecular components (i.e., H_2 and H_2O) in a novel clathrate structure (28). Additional work was done to constrain the full *P-T-X* phase diagram, but this was limited to below 30 GPa and 450 K (29). Computational studies have examined higher *P-T* conditions but have focused on the familiar H_2O composition as mentioned above (24–27). The miscibility of H_2 and H_2O at 2–70 GPa and 1,000–6,000 K has also been studied theoretically (30), but these do not correspond to the deepest regions within Uranus and Neptune. The extent to which hydrogen molecules dissociate and/or react (e.g., with H_2O) to form new stable solid and fluid phases at the deep interior conditions of Uranus and Neptune thus remains an open question. This study was conducted to identify phases in the H–O system, including their structures and physical properties, in order to provide a materials basis for understanding the anomalous magnetic fields of these planets.

Results

We began by examining H_2–H_2O mixtures to the deep interior pressures of Uranus and Neptune using an in-house quantum-mechanical material structure search CALYPSO method (31, 32). Our search uncovered the surprising stability of trihydrogen oxide (H_3O) at these compressions (Fig. 1*A*). The unit cell of the H_3O structure (space group *Cmca*) found here contains 64 atoms; its hydrogen–oxygen covalent framework has a H:O ratio of 2:1, with remaining hydrogen in the voids in the form of H_2 molecules. This clathratelike framework structure differs from those previously found experimentally or predicted theoretically at high pressures for H_2O (28, 34, 35). The basic structural unit hosts six distinct bond lengths and three different bond angles (Fig. 1*C*). Adjacent basic units are nested, four of which form the unit cell. The structure contains unusual H_2 dimers separated by 1.09 Å with a nearest-neighbor H–H distance of 0.65 Å at 500 GPa, which is significantly shorter than that of molecular hydrogen at ambient conditions (0.74 Å). Calculations of the enthalpy of formation

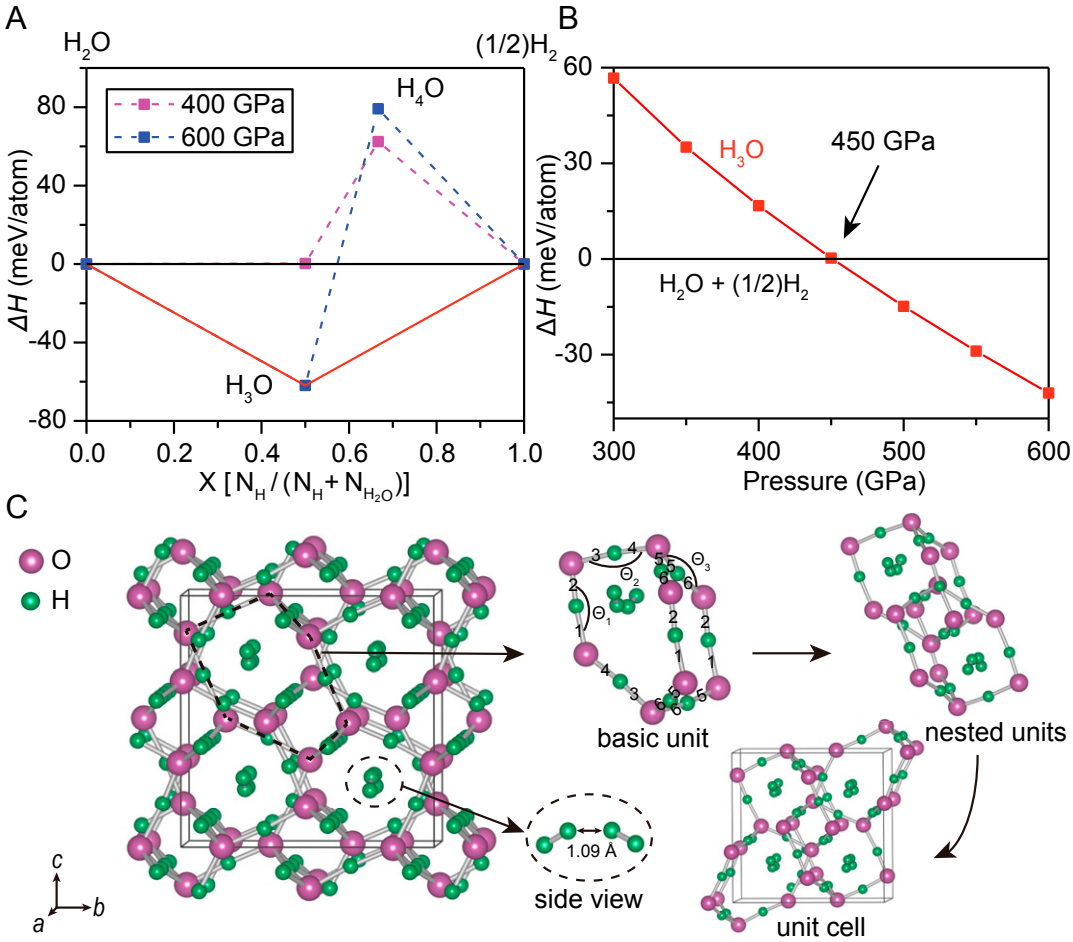

Fig. 1. Formation enthalpy and crystal structure of H_3O. (*A*) Formation enthalpy of H–O compounds with respect to decomposition into H_2O and H_2 at 400 and 600 GPa. (*B*) Enthalpy including the effect of zero-point energy versus pressure for H_3O relative to the results for decomposed H_2O and H_2. (*C*) Crystal structure (space group *Cmca*) and basic structural units of H_3O. Lattice parameters at 500 GPa are a = 3.35 Å, b = 5.84 Å, and c = 5.80 Å. There are two inequivalent atomic positions for O and four for H: O1 at 8f (0.00, 0.16, 0.00) and O2 at 8f (0.50, 0.49, 0.34), H1 at 8f (0.00, 0.33, 0.07), H2 at 8f (0.00, 0.43, 0.34), H3 at 16g (0.76, 0.09, 0.09), and H4 at 16g (0.33, 0.24, 0.23). Six distinct bonds in the basic unit labeled 1 through 6 have lengths 1.16, 1.02, 1.08, 1.06, 1.06, and 1.10 Å, respectively, and three bond angles $\theta_1 = 174.6°$, $\theta_2 = 174.7°$, and $\theta_3 = 171.3°$. Adjacent basic units are nested to form the unit cell of the H_3O structure, which is controlled by the persistence both covalent bonding and repulsive interactions at these extreme conditions. The evolution of the O–H distances with pressure and temperature is shown in *SI Appendix*, Fig. S10. The *Pbcm* structured phase for H_2O at 400 and 600 GPa (37) is used for the construction of the convex hull. For hydrogen, the *Cmca*-4 structure at 400 GPa and $I4_1/amd$ structure (38) at 600 GPa are used.

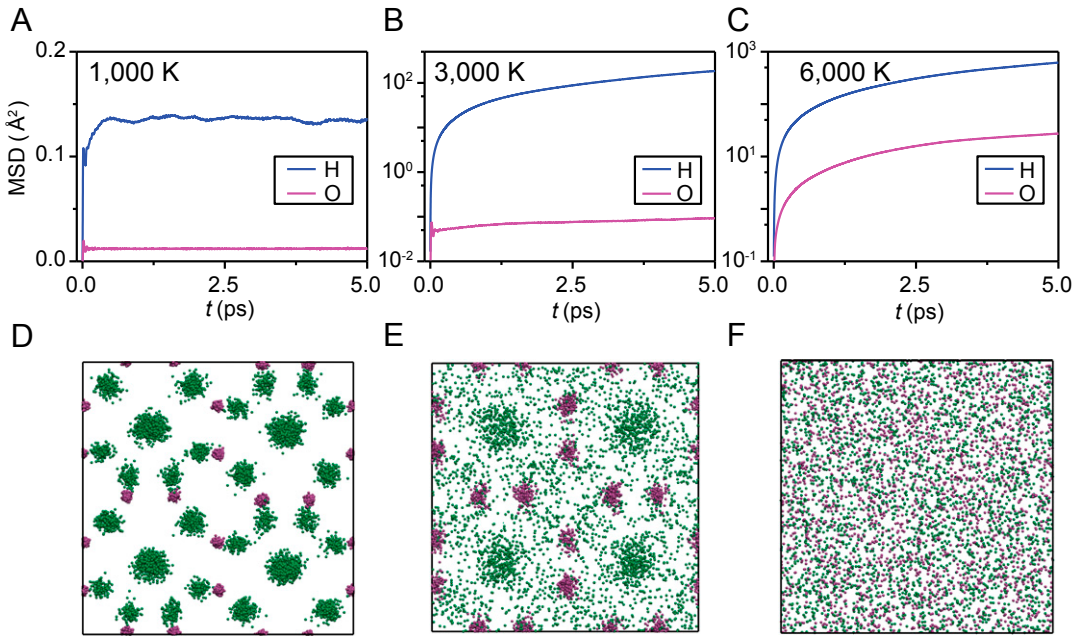

Fig. 2. Simulations of crystalline solid, superionic solid, and fluid phases of H_3O. (*A*–*C*) MSD of oxygen and hydrogen in H_3O at (*A*) 1,000 K, (*B*) 3,000 K, and (*C*) 6,000 K at a density of 4.30 g/cm^3, in three phases. (*D*–*F*) Trajectory snapshots of the corresponding phases, where the purple and green spheres represent instantaneous positions of oxygen and hydrogen atoms, respectively.

show that *Cmca*-H_3O is stable against decomposition to H_2O and H_2 above 450 GPa (Fig. 1*B*). The stability of an H_3O phase having this composition was previously reported (33, 36), but its structure is different and is stable at much higher pressure of 4.2 terapascals (TPa) (*SI Appendix*, Figs. S1–S3), which is far above the pressure range (0.4–0.6 TPa) considered in our study and not relevant to Uranus and Neptune. Our simulations are thus not in contradiction with the previous results obtained for the system at higher pressures (33, 36).

The onset of stability of H_3O lies within the pressures of 20–600 GPa estimated for the ice layers of Uranus and Neptune. Because of the high temperatures that also prevail within these planetary interiors, we examined the *P-T* phase stability and behavior using ab initio molecular dynamics (AIMD) simulations. Fig. 2 shows simulated mean-square displacement (MSD) and trajectory of H_3O at a density of 4.30 g/cm^3. At 1,000 K, MSD values of the hydrogen and oxygen atoms remain nearly constant (Fig. 2*A*), showing that the system is stable in the solid with all atoms near their equilibrium positions (Fig. 2*D*). At 3,000 K, the hydrogen atom MSD values begin to increase, whereas those of the oxygen atoms remain nearly constant (Fig. 2*B*), which signals a transition into a superionic state. This observation of a transition in the solid is corroborated by trajectory data, which also show that the oxygen atoms remain near their equilibrium positions while hydrogen atoms diffuse (Fig. 2*E*). On further increase in temperature (6,000 K), the oxygen atoms then diffuse, indicative of melting (Fig. 2 *C* and *F*). These calculations thus show that H_3O transforms from a crystalline solid to superionic solid at 1,250 K at 4.30 g/cm^3, then to a fluid near 5,250 K (Fig. 3).

We also carried out AIMD simulations of H_2O at comparable densities and temperatures to compare with the behavior of H_3O. The H_2O calculations were carried out at 4.93 g/cm^3 and 5,000–8,000 K. We find that solid H_2O remains in a superionic state up to 7,000 K, where H_3O is a fluid under these conditions (e.g., Fig. 3). In addition, we performed AIMD simulations using a supercell initially containing 48 H_2O molecules (144 atoms) in the *Pbcm* structure (37) and 48 atoms of hydrogen in the $I4_1/amd$ structure (38) at 4.30 g/cm^3 and 7,000 K (*SI Appendix*, Fig. S4*A*). The results show that hydrogen atoms readily penetrate into the H_2O lattice (*SI Appendix*, Fig. S4*B*), giving a radial distribution function for the H–H_2O system that matches that of H_3O (*SI Appendix*, Fig. S4*C*). These results validate a scenario in which H_2O reacts with hydrogen to form H_3O at these and even more extreme planetary interior conditions (*SI Appendix*, Fig. S5).

The above results enable us to construct a *P-T* phase diagram of H_3O covering the conditions corresponding to the interiors of Uranus and Neptune (Fig. 3*A*). The phase boundaries separating the solid, superionic, and fluid states were determined by AIMD simulations. The boundary separating H_3O and its decomposition products (H_2O and H_2) at low temperatures was determined by the difference in Gibbs free energy calculated using the quasi-harmonic approximation (39). The isentropes of Uranus and Neptune pass through the stability field of the fluid phase of H_3O (i.e., above ~500 and ~510 GPa), indicating that fluid H_3O is viable deep inside these ice giants in a shell surrounding their proposed cores. From the estimated pressure–radius relationship for these planets (40), these calculations predict that fluid H_3O stably exists in a thin-shell zone of 0.32–0.39 *R* (Fig. 3*B*), where *R* is the total radius of the planet. The density of fluid H_3O at 0.32 *R* is close to 4.30 g/cm^3, which is similar to the density of Uranus at the same radius (4.12 g/cm^3) (40).

Electrical conductivity is crucial to understanding planetary magnetic fields generated by the planetary dynamo. To that end, we also calculated the electronic structure and electrical transport properties of these materials. Calculations of the electronic band gap show that H_3O has a lower metallization temperature (~5,000 K at 540 GPa) than H_2O (~6,000 K at 590 GPa) (*SI Appendix*, Fig. S6*A*). These results indicate that H_3O becomes a metallic fluid in the deep mantle conditions of Uranus and Neptune. In contrast, H_2O remains in a superionic state and does not become a metallic fluid at these *P-T* conditions (up to 7,000 K and 600 GPa); rather, in the presence of hydrogen it reacts to produce H_3O. Further, the calculated electrical conductivity of H_3O shows an abrupt increase between 5,000 and 6,000 K, i.e., from 19 to 164 $(\Omega\ \text{cm})^{-1}$ (*SI Appendix*, Fig. S6*B*), which is consistent with the band-gap results. In contrast, the

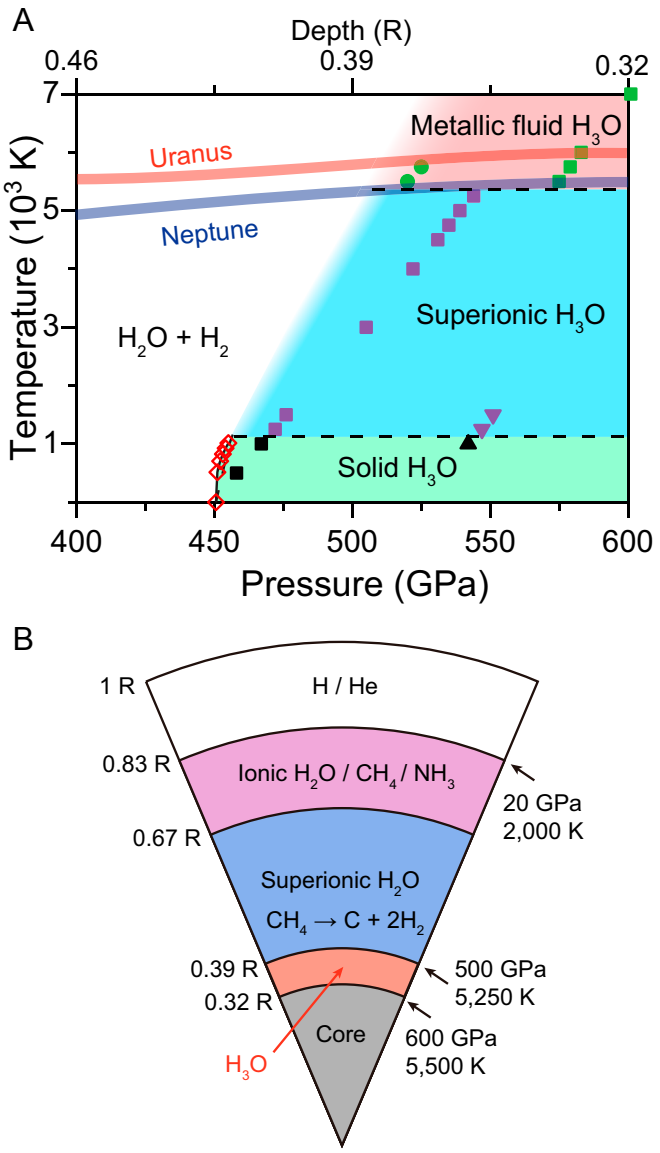

Fig. 3. The pressure–temperature phase diagram of H_3O in relation to the interiors of Uranus and Neptune. (*A*) Stability fields separating $H_2O + H_2$ and solid, superionic, and metallic liquid phases of H_3O, obtained from AIMD simulations. The blue and red solid lines indicate proposed isentropes of Neptune and Uranus (25), with the depth axis referring to the former. The filled circle, filled square, and filled triangle data points are AIMD simulation results at 4.14, 4.30, and 4.52 g/cm^3, respectively. (*B*) Possible schematic interior structure of Neptune. The gray and white regions represent the core and outer gas layers, respectively. The purple, blue, and orange areas represent regions dominated by ionic H_2O, superionic H_2O, and liquid H_3O, respectively. We emphasize that the boundaries shown are schematic and could be diffuse, and additional stratification cannot be ruled out (41). The pressure–radius relation was extracted from the estimate in ref. 40.

electrical conductivity of H_2O is found to be an order of magnitude lower than that of H_3O above 6,000 K, and no sudden changes in electrical conductivity are found for H_2O (*SI Appendix*, Fig. S6*B*). This metallization of H_3O on melting thus parallels that found for other materials such as silicon (42), diamond (43), and nitrogen (44).

Discussion

The principal result of this study is the unexpected finding of the high degree of stability of H_3O at *P-T* conditions that correspond to the deep interiors of Uranus and Neptune. The results are based on accurate and well-tested quantum simulations that have been validated for a variety of materials, in particular for low-Z materials, at extreme *P-T* conditions (e.g., refs. 19, 31, 32, and 45–48). Our AIMD simulations have not taken into account nuclear quantum effects for the hydrogens, the accurate determination of which requires substantial additional simulations. Although this is beyond the scope of the present work, the main conclusions regarding the predicted high degree of stability for H_3O at the conditions explored are not expected to change since the simulated temperatures are higher than its Debye temperature (2,700 K at 500 GPa). This assessment is consistent with our previous studies of quantum effects in pure hydrogen and other hydrogen-rich systems at extreme conditions (48, 49).

The calculated *P-T* stability of H_3O, together with its density and electrical conductivity under conditions at the base of the mantles of these planets, provide a materials basis for the underlying mechanism of their corresponding dynamos, specifically, for the thin-shell structure model conjectured for their planetary dynamos (5–8). Fluids with high electrical conductivity are essential to generating planetary magnetic fields (11). Our calculations reveal that the electrical conductivity of H_3O reaches 164 $(\Omega\ \mathrm{cm})^{-1}$ at 6,000 K, an order of magnitude larger than the value of ~20 $(\Omega\ \mathrm{cm})^{-1}$ for ionic ice that has been proposed to be responsible for the magnetic field of Uranus (13). Given that fluid H_3O is also more capable of convection than superionic solid ice, whose viscosity is expected to be several orders of magnitude larger than that of typical fluids, H_3O is also more conducive to producing magnetic fields.

Another consideration concerns the effects of element partitioning and fluid miscibility. Ice layer compositional models for Uranus and Neptune mentioned above correspond to $H_{35}O_7N$ (12) and $H_{28}O_7N$ (41), or a hydrogen–oxygen composition of H_5O and H_4O, respectively. It has been suggested that H_2O and H_2 can mix in all proportions in the fluid or plasma state at extreme conditions (30). On the other hand, the stability of H_3O in both solid and fluid phases predicted here and its similar density compared to that of the deep mantles inferred for Uranus and Neptune suggest a fluid metal with a composition close to that of H_3O. Indeed, the difference in densities (4.30 g/cm^3 calculated for H_3O versus 4.12 g/cm^3 inferred for the planets at the base of their mantles) can be explained by partitioning of other elemental components, including light elements C and N as well as heavier elements due to reactions with the proposed core.

Other materials models have been suggested for these planetary magnetic fields, including those arising from other complex metallic mixtures in their interiors as well as fluid hydrogen metallization (11, 41, 50, 51). The finding that H_3O is stable over a broad range of the deep interiors of Uranus and Neptune indicates that any of these proposed models needs to take into account this species, even as a possible core component. We note that our proposal of a dominant H_3O component at depth in ice giant planets is independent of whether the core is discrete (7), stably stratified (41), or diffuse as proposed for gas giants (52); the component could also be present at shallower depths in combination with other elements. These questions as well as the effects on melting and subsolidus phase relations for this multicomponent system at these extreme conditions remain to be studied. Moreover, the present predictions are within the range of current dynamic compression techniques (23, 53), and are thus expected to guide the design of experiments to test the theoretical results. The experiments should lead to improved understanding of the detailed structure of these unusual magnetic fields in terms of the component materials, specifically the geometry of the field represented as a strong displaced dipole.

There are also implications for other planets given that H_3O is found to be stable at more extreme *P-T* conditions than those found within Uranus and Neptune, including the variety of Neptune-like objects and for "water worlds" being discovered in

exoplanet searches (54, 55). For example, OGLE-2008-BLG-092L (56), a planet with four times the mass of Uranus, would support an even thicker region of metallic H_3O within its interior. Fluid metallic H_3O would also be expected to be a component of gas giant interiors but detailed consideration of this possibility requires further study of its thermodynamic and transport properties at more extreme conditions.

Conclusions

Given that hydrogen and oxygen are the first and third most abundant elements in the solar system, a consideration of their chemical interactions over a broad range of *P-T* conditions is required to understand the interior composition, structure, and processes of large planetary bodies. Extensive detailed quantum-mechanical simulations reveal the stability of H_3O at conditions corresponding to the deep interiors of Uranus and Neptune and indicate the importance of considering this chemical component for interior models of these planets. The stability, density, and electrical conductivity of fluid metallic H_3O are an order of magnitude larger than those of H_2O ice phases that have been proposed to be responsible for these magnetic fields. The results for the fluid metallic phase, in particular, provide a materials basis for the thin-shell dynamo model proposed to explain the magnetic field anomalies of Uranus and Neptune. Moreover, the theoretical results correspond to a *P-T* range that is accessible by current experimental techniques, and thus should guide future laboratory studies. The chemistry predicted at these extreme conditions will also be useful for developing accurate materials-based models for exoplanets, including the variety of Neptune-like objects that are being discovered.

Methods

Extensive structure searches were conducted using a swarm-intelligence-based CALYPSO method and code, which enables global structure searching in conjunction with ab initio energetic calculations. This method has been benchmarked on various known systems (45–47, 57). Density-functional (DF) theory calculations were performed using the Vienna Ab initio Simulation Package (VASP) plane-wave code (58, 59), where the Perdew-Burke-Ernzerhof (PBE) generalized gradient approximation DF (60) and frozen-core all-electron projector-augmented wave potentials (61) are adopted. The cutoff radius of the pseudopotentials for oxygen and hydrogen were 0.58 and 0.42 Å, respectively. To ensure validity of the adopted pseudopotentials, we also performed full-potential all-electron calculations for the equation of state for H_3O over the pressure range studied here using the WIEN2K code (62). The VASP calculation results were nearly identical to those obtained from all-electron calculations (*SI Appendix*, Fig. S7), validating the use of the pseudopotentials up to 600 GPa. The electronic wave functions were expanded in a plane-wave basis set with a kinetic energy cutoff of 1,200 eV, and the Brillouin zone (BZ) sampling was on *k* meshes with a reciprocal space resolution of $2\pi \times 0.032$ Å^{-1} to ensure that energies were converged to 1 meV/atom. The phonon calculations were performed with the Phonopy code (63) using a finite-displacement approach (64).

The AIMD simulations were performed in the canonical (*NVT*) ensemble applying a Nosé thermostat. A system containing 128 atoms was used for H_3O. Simulations reach 15 ps, with the first 2–5 ps for equilibrating the system. The time step was chosen to be 0.5 fs, and a $2 \times 2 \times 2$ *k*-mesh grid is used for the BZ sampling. To check for size effects, a larger system with 576 atoms was adopted. The transition temperature of this larger system was the same as for the smaller system, confirming convergence regarding system size. The simulated temperatures ranged from 1,000 to 7,000 K with a temperature step of 500 K, and we chose the temperature step in the regions of interest (1,000–1,500 K and 5,000–6,000 K) to be 250 K to investigate the temperatures for phase transitions from the crystalline solid to the superionic phase, and then to the fluid. The simulation cell for H_2O contained 144 atoms. The Gibbs free energy (*G*) was calculated using the quasiharmonic approximation by the Phonopy code. *G* is defined at a constant *T* and *P* by the formula: $G(T,P) = \min_V [U(V) + PV + F_{\text{phonon}}(T,V)]$, where *U* is the internal lattice energy, *V* is volume, and F_{phonon} is the phonon free energy. $F_{phonon}(T,V) = k_B T \int_0^\infty g(\omega,V) \ln\left[2\sinh\left(\frac{\hbar\omega}{2k_BT}\right)\right] d\omega$, where $g(\omega,V)$ is the phonon density of states at frequency ω and volume *V*. The minimal value of *G* was found at the equilibrium volume for a given *T* and *P*.

The time-averaged valence-conduction electronic band gap was calculated using the PBE functional (50 configurations for averaging) and cross-checked using the *GW* method (65) (10 configurations for averaging). For *GW* calculations, a $2 \times 2 \times 2$ *k*-mesh grid was used for balancing accuracy and efficiency (*SI Appendix*, Fig. S6). The PBE and *GW* calculations were in good agreement, and gave consistent results for H_3O reaching the metallic state under the same *P-T* conditions (*SI Appendix*, Fig. S9). The time-averaged direct current electrical conductivity was calculated via the Kubo–Greenwood formula (66, 67). using the KGEC code (68), which is a postprocessor module for use with the Quantum Espresso package (69). To obtain converged conductivity results, 576 atoms for H_3O and 540 atoms for H_2O were used in the simulation. A $3 \times 3 \times 3$ *k* mesh was used for BZ sampling. The conductivity values were determined from averaging over 10 configurations.

Data Availability Statement. All data discussed in the paper are available upon request.

ACKNOWLEDGMENTS. We are grateful for constructive comments from the reviewers, S. Stanley, S. Zhang, and S. A. Gramsch. We acknowledge funding from the National Natural Science Foundation of China (Grants 11822404, 11774127, 11534003, and 11622432), Science Challenge Project TZ2016001, and Program for Jilin University Science and Technology Innovative Research Team (JLUSTIRT). We utilized computing facilities at the High-Performance Computing Center of Jilin University and Tianhe2-JK at the Beijing Computational Science Research Center. R.J.H. acknowledges support from the US National Science Foundation (Grant DMR-1809783).

1. I. De Pater, J. J. Lissauer, *Planetary Sciences* (Cambridge University Press, Cambridge, 2015).
2. N. F. Ness *et al*., Magnetic fields at Uranus. *Science* **233**, 85–89 (1986).
3. N. F. Ness *et al*., Magnetic fields at Neptune. *Science* **246**, 1473–1478 (1989).
4. W. B. Hubbard, J. J. MacFarlane, Structure and evolution of Uranus and Neptune. *J. Geophys. Res. B* **85**, 225–234 (1980).
5. M. Podolak, W. B. Hubbard, D. J. Stevenson, "Models of Uranus' interior and magnetic field" in *Uranus*, T. Bergstralh, E. D. Miner, M. S. Matthews, Eds. (University of Arizona Press, Tucson, 1991), pp. 29–61.
6. W. B. Hubbard, M. Podolak, D. J. Stevenson, "The interior of Neptune" in *Neptune and Triton*, D. P. Cruikshank, Ed. (University of Arizona Press, Tucson, 1995), pp. 125–154.
7. S. Stanley, J. Bloxham, Convective-region geometry as the cause of Uranus' and Neptune's unusual magnetic fields. *Nature* **428**, 151–153 (2004).
8. S. Stanley, J. Bloxham, Numerical dynamo models of Uranus' and Neptune's magnetic fields. *Icarus* **184**, 556–572 (2006).
9. D. J. Stevenson, Planetary magnetic fields: Achievements and prospects. *Space Sci. Rev.* **152**, 651–664 (2010).
10. C. A. Jones, Planetary magnetic fields and fluid dynamos. *Annu. Rev. Fluid Mech.* **43**, 583–614 (2011).
11. W. J. Nellis, The unusual magnetic fields of Uranus and Neptune. *Mod. Phys. Lett. B* **29**, 1430018 (2015).
12. W. B. Hubbard, Interiors of the giant planets. *Science* **214**, 145–149 (1981).
13. W. J. Nellis *et al*., The nature of the interior of uranus based on studies of planetary ices at high dynamic pressure. *Science* **240**, 779–781 (1988).
14. M. Ross, The ice layer in Uranus and Neptune—Diamonds in the sky? *Nature* **292**, 435–436 (1981).
15. T. Schindelback, M. Somayazulu, R. J. Hemley, H. K. Mao, Breakdown of methane at high pressures and temperatures. *Materials Research Society 1997 Fall Meeting Program* (1997), p. 583.
16. L. R. Benedetti *et al*., Dissociation of CH_4 at high pressures and temperatures: Diamond formation in giant planet interiors? *Science* **286**, 100–102 (1999).
17. G. Gao *et al*., Dissociation of methane under high pressure. *J. Chem. Phys.* **133**, 144508 (2010).
18. D. Kraus *et al*., Formation of diamonds in laser-compressed hydrocarbons at planetary interior conditions. *New Astron.* **1**, 606–611 (2017).
19. V. Naden Robinson, M. Marqués, Y. Wang, Y. Ma, A. Hermann, Novel phases in ammonia-water mixtures under pressure. *J. Chem. Phys.* **149**, 234501 (2018).
20. C. Cavazzoni *et al*., Superionic and metallic states of water and ammonia at giant planet conditions. *Science* **283**, 44–46 (1999).
21. H. F. Wilson, M. L. Wong, B. Militzer, Superionic to superionic phase change in water: Consequences for the interiors of uranus and neptune. *Phys. Rev. Lett.* **110**, 151102 (2013).
22. M. Millot *et al*., Experimental evidence for superionic water ice using shock compression. *Nat. Phys.* **14**, 297–302 (2018).
23. M. Millot *et al*., Nanosecond X-ray diffraction of shock-compressed superionic water ice. *Nature* **569**, 251–255 (2019).
24. M. French, T. R. Mattsson, R. Redmer, Diffusion and electrical conductivity in water at ultrahigh pressures. *Phys. Rev. B Condens. Matter Mater. Phys.* **82**, 174108 (2010).
25. R. Redmer, T. R. Mattsson, N. Nettelmann, M. French, The phase diagram of water and the magnetic fields of Uranus and Neptune. *Icarus* **211**, 798–803 (2011).
26. J.-A. Hernandez, R. Caracas, Superionic-superionic phase transitions in body-centered cubic H_2O Ice. *Phys. Rev. Lett.* **117**, 135503 (2016).

27. M. French, R. Redmer, Electronic transport in partially ionized water plasmas. *Phys. Plasmas* **24**, 092306 (2017).
28. W. L. Vos, L. W. Finger, R. J. Hemley, H. K. Mao, Novel H_2-H_2O clathrates at high pressures. *Phys. Rev. Lett.* **71**, 3150–3153 (1993).
29. W. L. Vos, L. W. Finger, R. J. Hemley, H. K. Mao, H. S. Yoder, "Phase behavior of H_2-H_2O at high pressure" in *High Pressure Science and Technology–1993*, S. C. Schmidt, J. W. Shaner, G. A. Samara, M. Ross, Eds. (AIP Press, New York, 1994), pp. 857–860.
30. F. Soubiran, B. Militzer, Miscibility calculations for water and hydrogen in giant planets. *Astrophys. J.* **806**, 228 (2015).
31. Y. Wang, J. Lv, L. Zhu, Y. Ma, CALYPSO: A method for crystal structure prediction. *Comput. Phys. Commun.* **183**, 2063–2070 (2012).
32. Y. Wang, J. Lv, L. Zhu, Y. Ma, Crystal structure prediction via particle-swarm optimization. *Phys. Rev. B Condens. Matter Mater. Phys.* **82**, 094116 (2010).
33. S. Zhang, H. F. Wilson, K. P. Driver, B. Militzer, H_4O and other hydrogen-oxygen compounds at giant-planet core pressures. *Phys. Rev. B Condens. Matter Mater. Phys.* **87**, 024112 (2013).
34. A. Hermann, N. W. Ashcroft, R. Hoffmann, High pressure ices. *Proc. Natl. Acad. Sci. U.S.A.* **109**, 745–750 (2012).
35. H. Liu, Y. Yao, D. D. Klug, Stable structures of He and H_2O at high pressure. *Phys. Rev. B Condens. Matter Mater. Phys.* **91**, 014102 (2015).
36. C. J. Pickard, M. Martinez-Canales, R. J. Needs, Decomposition and terapascal phases of water ice. *Phys. Rev. Lett.* **110**, 245701 (2013).
37. M. Benoit, M. Bernasconi, P. Focher, M. Parrinello, New high-pressure phase of ice. *Phys. Rev. Lett.* **76**, 2934–2936 (1996).
38. C. J. Pickard, R. J. Needs, Structure of phase III of solid hydrogen. *Nature Phys.* **3**, 473–476 (2007).
39. A. Togo, F. Oba, I. Tanaka, First-principles calculations of the ferroelastic transition between rutile-type and $CaCl_2$-type SiO_2 at high pressures. *Phys. Rev. B Condens. Matter Mater. Phys.* **78**, 134106 (2008).
40. R. Helled, J. D. Anderson, M. Podolak, G. Schubert, Interior models of Uranus and Neptune. *Astrophys. J.* **726**, 15 (2010).
41. R. Chau, S. Hamel, W. J. Nellis, Chemical processes in the deep interior of Uranus. *Nat. Commun.* **2**, 203 (2011).
42. I. Iida, R. I. L. Guthrie, *The Physical Properties of Liquid Metals* (Oxford University Press, New York, 1988).
43. J. H. Eggert *et al*., Melting temperature of diamond at ultrahigh pressure. *Nat. Phys.* **6**, 40–43 (2009).
44. S. Jiang *et al*., Metallization and molecular dissociation of dense fluid nitrogen. *Nat. Commun.* **9**, 2624 (2018).
45. J. Lv, Y. Wang, L. Zhu, Y. Ma, Predicted novel high-pressure phases of lithium. *Phys. Rev. Lett.* **106**, 015503 (2011).
46. F. Peng, M. Miao, H. Wang, Q. Li, Y. Ma, Predicted lithium-boron compounds under high pressure. *J. Am. Chem. Soc.* **134**, 18599–18605 (2012).
47. H. Wang, J. S. Tse, K. Tanaka, T. Iitaka, Y. Ma, Superconductive sodalite-like clathrate calcium hydride at high pressures. *Proc. Natl. Acad. Sci. U.S.A.* **109**, 6463–6466 (2012).
48. H. Liu *et al*., Dynamics and superconductivity in compressed lanthanum superhydride. *Phys. Rev. B* **98**, 100102 (2018).
49. H. Liu, Y. Ma, Proton or deuteron transfer in phase IV of solid hydrogen and deuterium. *Phys. Rev. Lett.* **110**, 025903 (2013).
50. W. J. Nellis, Magnetic fields of Uranus and Neptune: Metallic fluid hydrogen. *AIP Conf. Proc.* **1793**, 090002 (2017).
51. M. Guarguaglini *et al*., Equation of state and optical properties of shock-compressed C: H: N: O molecular mixtures. arXiv:1804.06595 (18 April 2018).
52. F. Debras, G. Chabrier, New models of Jupiter in the context of Juno and Galileo. *Astrophys. J.* **872**, 100 (2019).
53. P. M. Celliers *et al*., Insulator-metal transition in dense fluid deuterium. *Science* **361**, 677–682 (2018).
54. S. Dong, J.-W. Xie, J.-L. Zhou, Z. Zheng, A. Luo, LAMOST telescope reveals that Neptunian cousins of hot Jupiters are mostly single offspring of stars that are rich in heavy elements. *Proc. Natl. Acad. Sci. U.S.A.* **115**, 266–271 (2018).
55. T. Trifonov, J. Rybizki, M. Kürster, TESS exoplanet candidates validated with HARPS archival data: A massive Neptune around GJ 143 and two Neptunes around HD 23472. *Astron. Astrophys.* **622**, L7 (2019).
56. R. Poleski *et al*., Triple microlens OGLE-2008-BLG-092L: Binary stellar system with a circumprimary Uranus-type planet. *Astrophys. J.* **795**, 42 (2014).
57. L. Zhu, H. Liu, C. J. Pickard, G. Zou, Y. Ma, Reactions of xenon with iron and nickel are predicted in the Earth's inner core. *Nat. Chem.* **6**, 644–648 (2014).
58. G. Kresse, J. Furthmüller, Efficient iterative schemes for ab initio total-energy calculations using a plane-wave basis set. *Phys. Rev. B Condens. Matter* **54**, 11169–11186 (1996).
59. G. Kresse, J. Furthmüller, Efficiency of ab-initio total energy calculations for metals and semiconductors using a plane-wave basis set. *Comput. Mater. Sci.* **6**, 15–50 (1996).
60. J. P. Perdew, K. Burke, M. Ernzerhof, Generalized gradient approximation made simple. *Phys. Rev. Lett.* **77**, 3865–3868 (1996).
61. G. Kresse, D. Joubert, From ultrasoft pseudopotentials to the projector augmented-wave method. *Phys. Rev. B Condens. Matter Mater. Phys.* **59**, 1758–1775 (1999).
62. P. Blaha, K. Schwarz, P. Sorantin, S. B. Trickey, Full-potential, linearized augmented plane wave programs for crystalline systems. *Comput. Phys. Commun.* **59**, 399–415 (1990).
63. A. Togo, I. Tanaka, First principles phonon calculations in materials science. *Scr. Mater.* **108**, 1–5 (2015).
64. K. Parlinski, Z. Q. Li, Y. Kawazoe, First-principles determination of the soft mode in cubic ZrO_2. *Phys. Rev. Lett.* **78**, 4063–4066 (1997).
65. M. Shishkin, G. Kresse, Implementation and performance of the frequency-dependent GW method within the PAW framework. *Phys. Rev. B Condens. Matter Mater. Phys.* **74**, 035101 (2006).
66. E. R. Hernández, A. Rodriguez-Prieto, A. Bergara, D. Alfè, First-principles simulations of lithium melting: Stability of the bcc phase close to melting. *Phys. Rev. Lett.* **104**, 185701 (2010).
67. D. A. Greenwood, The Boltzmann equation in the theory of electrical conduction in metals. *Proc. Phys. Soc.* **71**, 585–596 (1958).
68. L. Calderín, V. V. Karasiev, S. B. Trickey, Kubo–Greenwood electrical conductivity formulation and implementation for projector augmented wave datasets. *Comput. Phys. Commun.* **221**, 118–142 (2017).
69. P. Giannozzi *et al*., QUANTUM ESPRESSO: A modular and open-source software project for quantum simulations of materials. *J. Phys. Condens. Matter* **21**, 395502 (2009).